

Green’s-Function Spherical Neural Operators for Biological Heterogeneity

Hao Tang¹, Hao Chen², Hao Li³, Chao Li^{1,2}

¹University of Dundee, United Kingdom.

²University of Cambridge, United Kingdom.

³Fudan University, China.

Abstract

Spherical deep learning has been widely applied to a broad range of real-world problems. Existing approaches often face challenges in balancing strong spherical geometric inductive biases with the need to model real-world heterogeneity. To solve this while retaining spherical geometry, we first introduce a designable Green’s function framework (DGF) to provide new spherical operator solution strategy: Design systematic Green’s functions under rotational group. Based on DGF, to model biological heterogeneity, we propose **Green’s-Function Spherical Neural Operator** (GSNO) fusing 3 operator solutions: (1) Equivariant Solution derived from Equivariant Green’s Function for symmetry-consistent modeling; (2) Invariant Solution derived from Invariant Green’s Function to eliminate nuisance heterogeneity, e.g., consistent background field; (3) Anisotropic Solution derived from Anisotropic Green’s Function to model anisotropic systems, especially fibers with preferred direction. Therefore, the resulting model, GSNO can adapt to real-world heterogeneous systems with nuisance variability and anisotropy while retaining spectral efficiency. Evaluations on spherical MNIST, Shallow Water Equation, diffusion MRI fiber prediction, cortical parcellation and molecule structure modeling demonstrate the superiority of GSNO.

Keywords: Green’s function, spherical convolution, spherical harmonics, neural operator

1 Introduction

Deep learning on spherical domains has become essential in scientific and engineering disciplines where data naturally resides on curved manifolds. These include applications ranging from planetary-scale simulations in Earth science [1–5], brain mapping in neuroscience [6–12], omnidirectional perception in computer vision [13–17], and molecular structure learning in biology and chemistry [18–23]. These applications require models respecting spherical geometry to avoid distortions or coordinate-dependent artifacts, while remaining expressive enough to capture heterogeneous, spatially varying, and often nonlinear phenomena that characterize real-world spherical systems.

A broad range of methods has been developed to meet these demands. Planar-projection CNNs [24–28] adapt Euclidean models to spherical tasks but inevitably introduce grid distortions and break spherical geometry, limiting performance on sphere-native tasks [19, 29–31]. More recent graph-based [32–36] and Transformer-based [37–43] spherical models enhance spatial adaptability and nonlinear modeling, yet often embed the sphere as an unstructured graph or sequence, compromising spherical geometric consistency and incurring substantial computational cost [27, 44, 45]. These approaches enhance expressivity but lack a coherent principle for balancing symmetry and heterogeneity.

Harmonic-based and group-equivariant methods address geometric fidelity by enforcing rotational equivariance through spherical convolutions [46–49]. They underpin spherical CNNs applied to brain cortical analysis [9, 50–52], fiber prediction [11, 12, 53], as well as spherical Fourier neural operators (SFNOs) for climate and geophysical dynamics [54–57]. While such models efficiently capture global interactions and provide strong inductive biases [19, 29, 58–60], the assumption of strict rotational equivariance often fails to model real-world systems that deviate substantially from ideal isotropy and rotational symmetric group $SO(3)$, e.g., atmospheric fields with latitude-dependent dynamics and terrain-induced invariance; diffusion MRI showing microstructural anisotropy. Strict equivariance can therefore suppress essential local structure, leading to underfitting and reduced generalization [30, 61–64]. Attempts to break rotational equivariance via activation functions, linear layers, positional encoding, and hybrid pooling [3, 65–70] still remain aspheric native, heuristic or task-specific. A principled solution integrating equivariant inductive bias with real-world adaptability remains challenging.

This work aims to address the adaptability required to represent the complex, heterogeneous real-world spherical systems that do not adhere to the symmetry $SO(3)$ -group. We propose the Green’s function Spherical Neural Operators (GSNO), fusing Equivariant, Invariant and Anisotropic components to simulate heterogeneous biological systems. We first establish a Designable Green’s Function Framework (DGF) to construct a new class of spherical operators. Based on this framework, we design three Green’s functions and derive the corresponding solution operator for different systems: (1) Equivariant Green’s function $G_E(R^{-1}u)$ based on the relative position \rightarrow Existing Equivariant Operator for isotropic symmetry modeling; (2) Invariant Green’s function $G_I(u)$ based on the absolute position \rightarrow A new Invariant Operator for invariance modeling; (3) Anisotropic Green’s function $G_A(u \cdot Rd)$ based on the learnable directions \rightarrow A new Anisotropic Operator with learnable symmetry groups $SO(\theta)$ for anisotropy

modeling. The three solution operators are concatenated to form GSNO for efficient heterogeneous modeling.

We evaluate GSNO across diverse tasks in physical, biomedical, and computational domains, including strictly symmetric (molecular QM7 potentials), where equivariance must be preserved; partially symmetric (cortical parcellation), where global structure coexists with localized anisotropy; and strongly heterogeneous (weather forecasting, shallow-water simulations and fiber orientation), where symmetry is heavily violated. Across all benchmarks, GSNO consistently outperforms comparison methods. Ablation studies reveal that the corrective term enhances performance specifically in heterogeneous regimes, while maintaining equivariant behaviour when symmetry is present. These results suggest our approach achieves superior generalization, parameter efficiency, and robustness, particularly in heterogeneous or nonlinear regimes. Our main contributions are summarized as:

1. A designable Green’s function framework (DGF) to design different operators.
2. Three spherical operators derived from 3 Green’s functions, especially the new Invariant and Anisotropic Operators for biological heterogeneity.
3. Propose GSNO by fusing different types of operators for spherical system modeling.
4. Extensive experiments across diverse systems, demonstrating the performance of different operators and GSNO.

Together, these contributions provide a rigorous and practically robust foundation for spherical operator learning, aligning geometric fidelity with the complexity of real-world spherical systems while overcoming the fundamental limitations of strictly isotropic and equivariant models.

2 Results

2.1 Study design

Designable Green’s Function Framework:

Figure 1(A) shows the real solution to a real spherical linear system. Specifically, for a differential operator system defined on the sphere:

$$D(g(u)) = f(u), \quad u \in S^2, \tag{1}$$

where $f(u)$ is the input function and $g(u)$ is the target. By defining the spherical Green’s function $G(u, R)$ of the system [71], derive the solution of this system as:

$$g(u) = \int_{S^2} G(u, R) f(Rn) dR, \tag{2}$$

where R is an element of the three-dimensional rotation group $SO(3)$ and n is the north pole.

Fig.1 (A) shows the real solution to spherical systems based on Green’s function method. In the proposed Designable Green’s Function Framework (DGF) shown in the

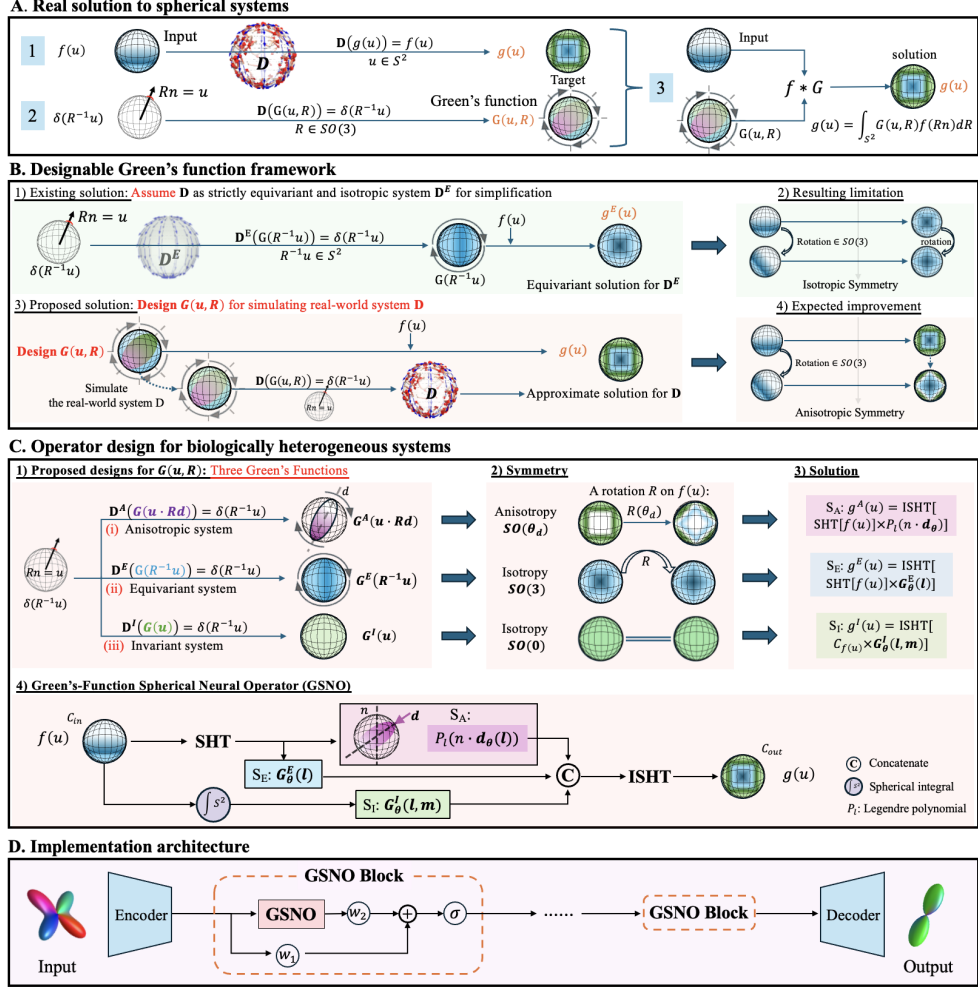


Fig. 1 The proposed DGF and GSNO. SHT and ISHT represent spherical harmonic transform and inverse transform. w is the linear layer and σ is the activation function.

Fig.1 (B), we demonstrates the underlying limitation of existing simplified solution: Systematic isotropy and equivariance limit the real-world system modeling. To solve this, we propose to design new Green's functions to simulate real-world systems while retaining strictly sphere-native.

Equivariant Operator from $G(R^{-1}u)$:

We design $G(R, u)$ as $G(R^{-1}u)$, and apply the spherical convolution theorem [3, 19, 47] to derive the equivariant operator solution with $SO(3)$ -symmetry as:

$$\{G(u, R) : G(R^{-1}u)\} \rightarrow \{g^E(u) = \text{ISHT}[G_\theta(l) \cdot \text{SHT}[f]_l^m]\}, \quad (3)$$

where $G_\theta(l)$ denote the learnable, symmetrical kernel in spectral domain. SHT and ISHT is the spherical harmonic transform and the inverse transform. This design enforces strict isotropy and equivariance to achieve efficient global modeling, but ignores heterogeneity, especially invariance and anisotropy, as shown in Figure 1(B).

Invariant Operator from $G(u)$:

To explicitly model invariant physics, such as fixed terrain, the same MRI protocol, and the invariance required for classification/segmentation tasks, we design the Invariant Green’s Function G^I and derive the invariant operator solution:

$$\{G(R, u) : G(u)\} \rightarrow \{g^I(u) = \text{ISHT}[C_f \cdot G_\theta^2(l, m)]\}, \quad (4)$$

where C_f is the spherical integral of the input function $f(u)$.

Anisotropic Operator from $G(u \cdot Rd)$:

To explicitly model anisotropy, especially the local directionality existing at the boundaries of cortical partitions and the inherent anisotropy of nerve fibers, we design the Anisotropic Green’s Function G^A and derive the anisotropic operator solution:

$$\{G(R, u) : G(u \cdot (Rd))\} \rightarrow \{g^A(u) = \text{ISHT}[P_L(n \cdot \mathbf{d}_\theta) \cdot \text{SHT}[f]^m]\}, \quad (5)$$

where P_L is the L -th order Legendre polynomial, \mathbf{d}_θ is the learnable orientations.

Green’s-Function Spherical Neural Operator:

As shown in the Figure 1 (C and D), we design Green’s-Function Spherical Neural Operator (GSNO), a new spectral learning fusing Equivariant, Invariant and Anisotropic Operators by concatenation to model biologically heterogeneous systems while retaining sphere-native.

2.1.1 Experimental design

We compare GSNO to other state-of-the-art methods for 5 spherical experimental scenarios with distinct system characteristics, involving various spherical sampling methods, resolutions, and application fields, to comprehensively evaluate the generalization of GSNO. For example, brain nerve fiber modeling and cortical parcellation emphasize GSNO’s ability to model biological heterogeneity, including invariance and anisotropy. And the different time scales and spatial scales in shallow water equation highlight the nonlinear and asymmetric modeling capability and stability of GSNO. Spherical digital recognition and atomic structure analysis demonstrate the generalization ability of GSNO for spherical symmetry systems. All experiments are implemented through PyTorch on 32GB V100 GPUs.

2.2 Synthetic Spherical Scenarios

We first validate GSNO on two synthetic spherical scenarios with different scales.

Table 1 ACC \uparrow (in %) on spherical mnist at different resolutions.

Method	Channel	Different Resolutions			
		32 \times 32	64 \times 64	128 \times 128	256 \times 256
CNN	256	98.1	98.1	98.3	98.2
Spherical CNN	64	95.1	95.3	95.6	95.8
SFNO	256	97.3	97.4	98.9	99.1
GSNO (Ours)	256	99.3	99.4	99.6	99.7

Table 2 MRE \downarrow ($\times 10^{-3}$) on SSWE at different spatial resolutions and prediction horizons. Bold indicates the best performance.

Method	Prediction Horizon															
	5 h				10 h				15 h				20 h			
	32 \times 64	64 \times 128	128 \times 256	256 \times 512	32 \times 64	64 \times 128	128 \times 256	256 \times 512	32 \times 64	64 \times 128	128 \times 256	256 \times 512	32 \times 64	64 \times 128	128 \times 256	256 \times 512
FNO	0.72	0.82	1.97	2.59	1.00	1.30	2.24	3.36	1.55	1.63	2.71	4.47	1.59	1.82	3.04	5.14
SFNO	0.59	0.55	0.68	0.65	0.74	0.70	0.79	0.72	1.04	0.87	0.88	0.86	1.37	1.12	1.00	0.98
GSNO	0.47	0.50	0.62	0.60	0.59	0.59	0.67	0.64	0.78	0.62	0.69	0.67	0.99	0.66	0.77	0.86

2.2.1 Spherical MNIST

Spherical MNIST is a simulated dataset of handwritten digits on the sphere [19]. The native 28 \times 28 images are projected onto 32 \times 32, 64 \times 64, 128 \times 128 and 256 \times 256 equirectangular spherical grids through backward ray-casting and bilinear interpolation, yielding a rotation-free spherical MNIST benchmark at the four target resolutions while preserving the original 60 k / 10 k train-test split. Under the fixed view of spherical MNIST, GSNO achieves more accurate digital classification.

2.2.2 Shallow Water Equation

Spherical Shallow Water Equations (SWE) form a nonlinear hyperbolic PDE system that models the motion of thin-layer fluids on a rotating sphere. The core underlying assumption is the shallow water approximation, where the vertical scale of the fluid layer is much smaller than the horizontal scale [72]. Following [3, 72], we generate the SWE simulation using a classical spectral solver [73]. Four SWE datasets are generated with 4 spatial resolution of 32 \times 64, 64 \times 128, 128 \times 256, 256 \times 512; time step of 150 s; 3 channel dimensions: geopotential height (H), vorticity (V), and divergence (D). All the models use the identical dataset and setting: 50 epochs containing 256 samples each, batch size of 4, Adam optimizer with learning rate of 2×10^{-3} , and spherical weighted mean relative loss. Models are tested on the dataset generated from 50 initial conditions (50 samples) and evaluated using MRE for each variable. The results in the Table 2 show that GSNO achieves better performance on all variables and time scales.

2.3 Real-world Spherical Scenarios

We further validate the generalization of GSNO on multiple real-world heterogeneous systems.

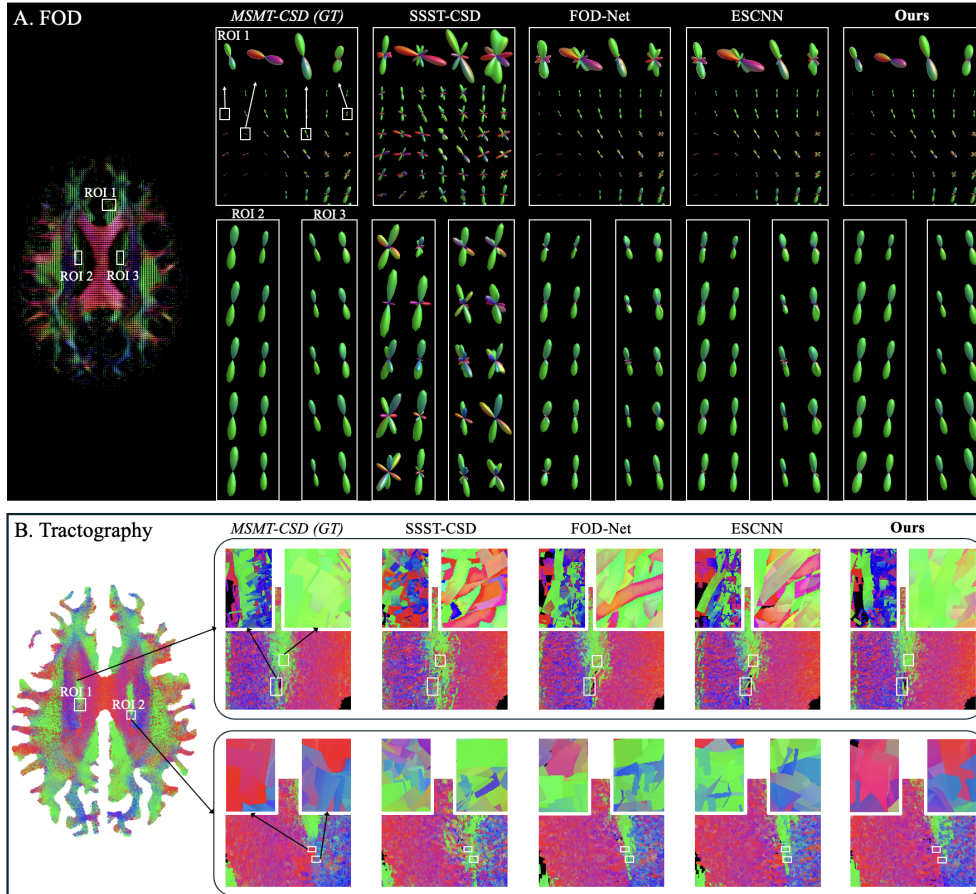


Fig. 2 FOD and Tractography on hcp dataset.

2.3.1 Diffusion MRI-based fiber estimation

Diffusion MRI (dMRI) modeling of brain microstructure is a distinct challenge in: (1) the input signals are sparse and anisotropic diffusion measurements acquired over spherical shells, exhibiting sharp angular variations corresponding to underlying fiber tract orientations; (2) the spatial sampling of dMRI-based fiber orientation distribution is performed using HEALPix, resulting in nonuniform and incomplete coverage of the spherical domain.

We randomly select dMRI images of 30 subjects in the Human Connectome Project (HCP) [77], where 20 subjects were for training, 5 for validation, and 5 for test. The complete dMRI data of each subject contains 288 volumes (multi-shell HARDI), including 270 volumes of $b=1000, 2000, 3000 \text{ s/mm}^2$ with 90 gradient directions for each shell and 18 b_0 volumes. Due to the wide application of low b -value with 32 gradient directions in clinical practice [75], we subsample 32 volumes of $b=1000$ and

Table 3 Performance comparison on HCP dataset for brain nerve fiber modeling (ACC \uparrow). Bold represents the best result.

Methods	SSMT-CSD [74]	FOD-Net [75]	ESCNN [76]	GSNO
Parameters	–	19.44 M	1.47 M	1.11 M
White matter	0.7523 \pm 0.0256	0.8858 \pm 0.0138	0.9006 \pm 0.0142	0.9176 \pm 0.0134
Whole brain	0.6640 \pm 0.0145	0.8250 \pm 0.0159	0.8362 \pm 0.0162	0.8590 \pm 0.0123

1 volume of b0 from the complete dMRI according to the HCP protocol, to obtain single-shell LARDI. Further, we use MSMT-CSD [78] on the multi-shell HARDI to obtain high angular resolution fiber orientation distribution (FOD) as the ground truth (HAR-FOD). Meanwhile, we use SSMT-CSD [74] on the single-shell LARDI to obtain single-shell low angular resolution FOD as the condition of GSNO (LAR-FOD). l_{max} is set to the default value of 8 to balance precision and complexity [75].

SSMT-CSD [74], FOD-Net [75], ESCNN [76] and our proposed GSNO adopt the same network architecture as FOD-Net. The difference lies in that FOD-Net uses 3D convolutional layers to handle a large number of harmonic coefficients, while ESCNN and GSNO stack voxels on the channel dimension and then use the spherical operator for learning. To ensure a fair comparison, these methods have exactly the same hyperparameters, with the only difference being the types of operators. The results of Angular Correlation Coefficient (ACC) [75] in Table 4 show that GSNO consistently outperforms other models, demonstrating strong generalization under irregular sampling and data sparsity. Especially, Figure 2 shows some regions of interest taken from the caudate nucleus and cingulate gyrus. Compared with the obviously false positive predictions by other methods, the proposed GSNO achieves more precise prediction of fiber orientation and density, especially for the inhibition of false fibers.

2.3.2 Cortical parcellation

Cortical parcellation requires both equivariance to handle large-scale spatial variations among individuals and biological heterogeneity modeling to capture nuisance variability and the local subtle features that determine the boundaries. This study evaluate the GSNO’s robustness to anatomical variability and its parcellation accuracy on the public Mindboggle-101 [79] and NAMIC-39 [80] datasets. The datasets comprises cortical surfaces with expert manual annotations, from which we extracted geometric features and mapped them onto the sphere following a preprocessing pipeline consistent with SPHARM-Net [9, 80].

All the models are trained and tested using five repetitions of 9-fold cross-validation, with performance assessed by the Dice coefficient. Results demonstrate that GSNO outperforms SOTAs in parcellation accuracy with fewer learnable parameters, without relying on rigid alignment or data augmentation. As shown in the Figure 3, GSNO achieves more accurate predictions on some small regions with complex geometers, blurred boundaries or large anatomical variations. It is precisely because the discriminative features of these regions rely on asymmetric local contexts that our flexible heterogeneity modeling can capture them.

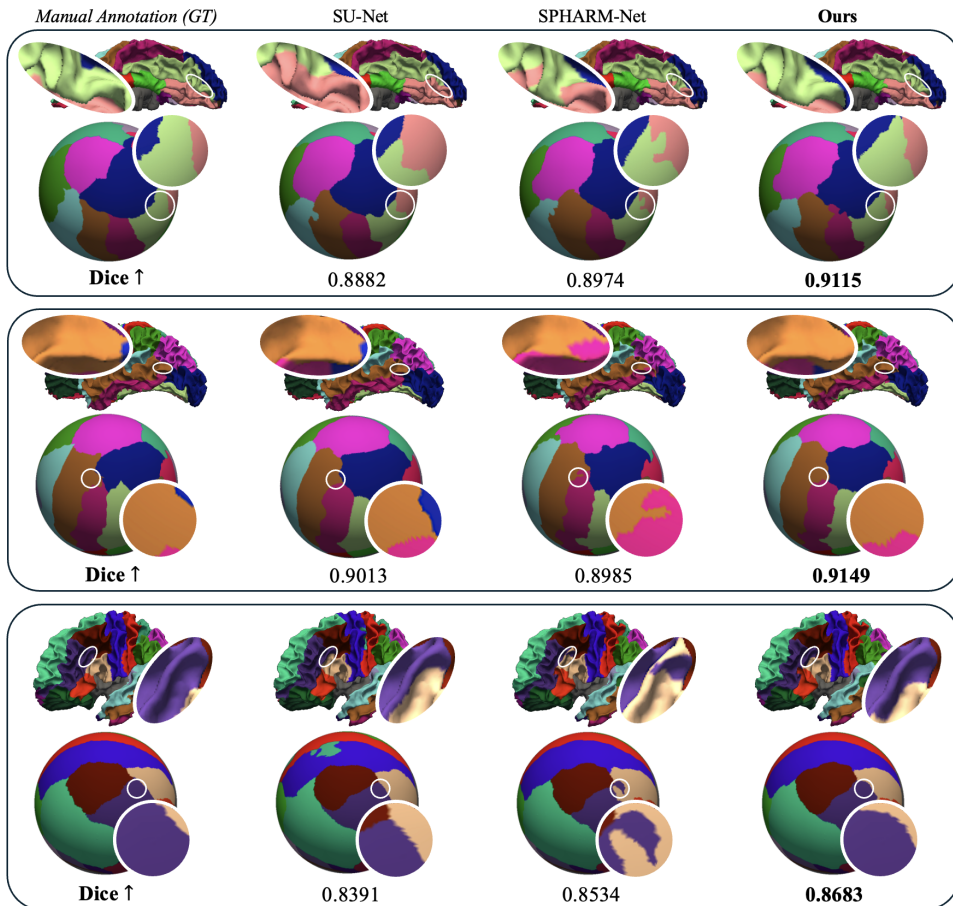


Fig. 3 Cortical parcellation on Mindboggle-101 and NAMIC-39 datasets.

Table 4 Performance comparison on Mindboggle-101 dataset for brain cortical parcellation (ACC and Dice \uparrow , in %). Bold represents the best result. (average of 1/3/5/7/9 in 9 folds)

Methods	SPHARM-Net-c64 [9]	SPHARM-Net-c128 [9]	Spherical U-Net [6]	GSNO-c64 (Ours)	GSNO-c128 (Ours)
Parameters	1.10 M	4.31 M	1.67 M	1.03 M	2.85 M
ACC	89.55	89.88	89.42	89.94	90.42
Dice	88.42	88.49	88.36	88.61	88.87

2.3.3 Molecule structure modeling

We further evaluate the generalization of GSNO on the QM7 benchmark, a energy-prediction dataset [81, 82] contains 7,165 molecules selected from GDB-13 chemical universe and optimized at the PBE0/def2-TZVP DFT level, providing 0 K atomization energies for neutral systems with up to 23 atoms of H, C, N, O and S. Each molecule is presented by placing non-overlapping spheres around atoms and computing 5-channel

Table 5 Performance comparison on NAMIC-39 dataset for brain cortical parcellation (ACC and Dice \uparrow , in %). Bold represents the best result. (average of 1/3/5/7/9 in 9 folds)

Methods	SPHARM-Net-c64 [9]	SPHARM-Net-c128 [9]	Spherical U-Net [6]	GSNO-c64 (Ours)	GSNO-c128 (Ours)
Parameters	1.10 M	4.32 M	1.67 M	1.03 M	2.85 M
ACC	89.65	89.79	89.42	89.77	90.28
Dice	85.31	85.36	84.66	85.40	85.82

Table 6 Performance comparison on QM7 for molecule feature analysis (RMSE \downarrow). Bold represents the best result.

Methods	mlp	Spherical CNN	GSNO(Ours)
Parameters	0.001 M	0.169 M	0.119 M
Average	16.06	8.47	3.51

Coulomb-type potential maps on the sphere (bandwidth = 10, Driscoll-Healy grid), yielding spherical geometry of molecule [19].

In this structurally heterogeneous system, subtle variations in local chemical environments and geometric configurations can induce large changes in global molecular energy. Moreover, molecular energies are invariant under rotations, requiring rotational symmetry. Training and testing follow the 5-fold cross-validation split consistent with spherical CNN [19]; Root mean squared error (RMSE) is used as evaluation metric. As shown in the Table 6, GSNO with lower parameters achieves more precise energy prediction, which demonstrates the powerful adaptive ability of GSNO in the molecule system with structurally heterogeneity and rotational symmetry.

3 Discussion

These extensive experiments verify the superiority of GSNO, which further the feasibility of the designable Green’s function framework, especially in simulating real-world heterogeneous systems. Specifically, the derived Invariant Solution is effective to eliminate nuisance heterogeneity, e.g., medical imaging protocol-related noise or anatomical landmarks. The derived Anisotropic Solution is efficient to model anisotropy, especially the white matter fibers with preferred directions.

4 Methods

4.1 Designable Green’s Function Framework

The Green’s function method offers a classical strategy to solve PDEs, where the solution is expressed as a convolution integral with the Green’s function as the kernel [83]. For the sphere-native solution, we define D , a linear differential operator on the sphere, and consider the following PDE:

$$D(g(u)) = f(u), \quad u \in S^2 \tag{6}$$

where $f(u)$ is the input function and $g(u)$ is the target solution. The spherical Green’s function G , associated with D , is defined by the property:

$$D(G(u, R)) = \delta(R^{-1}u) = \begin{cases} \infty, & Rn = u, \\ 0, & Rn \neq u, \end{cases} \quad (7)$$

where $\delta(\cdot)$ denoting the Dirac delta function defined on the sphere, and $R \in SO(3)$ represents a rotation from the north pole n . Using the Green function, the solution to Equation 6 is:

$$g(u) = \int_{S^2} G(u, R)f(Rn) dR \quad (8)$$

This solution is verified in our prior work [71]. By assuming any system/mapping as the solution of a differential equation: $f(u) \rightarrow g(u)$, we propose the **Designable Green’s Function Framework** (DGF) to design different Green’s functions to simulate the real-world systems and simplify Equation 8 to derive the corresponding operator solution $g(u)$.

4.2 Three Operators from three Green’s Functions

We design Equivariant Green’s Function $G(R^{-1}u)$, Invariant Green’s Function $G(u)$ and Anisotropic Green’s Function $G(u \cdot Rd)$ and derive their operator solutions.

4.2.1 Equivariant Operator from $G(R^{-1}u)$

Inspired by existing equivariant methods, we design $G(u, R)$ as $G^E(R^{-1}u)$ assuming strictly isotropic $SO(3)$ -symmetry to achieve strict rotational equivariance. Under this formulation, the prediction target $g(u)$ is given by:

$$g(u) = \int_{S^2} G^E(R^{-1}u)f(Rn) dR. \quad (9)$$

Applying the spherical convolution theorem [3, 19, 47], the spherical harmonics transform of $g(u)$ is derived as:

$$\begin{aligned} \text{SHT}[g(u)](l, m) &= \text{SHT}[(f * G^E)](l, m) \\ &= 2\pi \sqrt{\frac{4\pi}{2l+1}} \cdot \text{SHT}[G^E](l, 0) \cdot \text{SHT}[f](l, m). \end{aligned} \quad (10)$$

Thus, the operator solution $g(u)$ is reconstructed via the ISHT:

$$g(u) = \text{ISHT}(G_\theta^E(l) \cdot \text{SHT}[f](l, m)), \quad (11)$$

where $G_\theta(l)$ denote the learnable spectral weights parameterized by the neural operator.

4.2.2 Invariant Operator from $G(u)$

Motivation: Spherical biomedical systems—such as cortical surface measurements, diffusion-derived features, or functional activation maps—are often subject to substantial variability arising from acquisition protocols, coordinate choices, and inter-subject alignment procedures. These sources of variability induce differences in the observed data that do not reflect underlying biological differences. For instance, global rotations of the sphere, scanner-dependent orientation conventions, or arbitrary surface parameterizations can significantly alter the numerical representation of a sample while leaving its biological interpretation unchanged. If left unconstrained, learning-based models may allocate substantial representational capacity to capturing such variability, thereby conflating coordinate-dependent artefacts with meaningful biological signals. This leads to reduced generalization, poor reproducibility across datasets, and sensitivity to irrelevant transformations. From a scientific standpoint, these effects are undesirable, as they obscure the relationship between the learned representation and the biological system of interest.

To explicitly address this issue and model invariant physics, inspired by our prior work [71], we design the Invariant Green’s Function G^I :

$$G(u, R) = G^I(u) \tag{12}$$

Based on G^I , we derive the invariant operator solution under DGF:

$$\begin{aligned} \text{SHT}[g(u)](l, m) &= \int_{SO(3)} f(Rn) \left(\int_{S^2} \left[\sum_{l', m'} \text{SHT}[G^I]_{l'}^{m'} Y_{l'}^{m'}(u) \right] \overline{Y_l^m(u)} du \right) dR \\ &= \text{SHT}[G^I](l, m) \int_{SO(3)} f(Rn) dR \\ &= C_f \cdot G_\theta^I(l, m), \end{aligned} \tag{13}$$

where C_f is the spherical integral of the input function ($f(u)$). $G_\theta^I(l, m)$ is an asymmetric kernel. The invariant operators enforce that the model’s output or intermediate representations remain unchanged under a prescribed set of transformations, such as global rotations of the sphere. Functionally, this amounts to collapsing all observations related by these transformations into a single equivalence class in representation space.

Rather than attempting to learn invariance from data, the invariant operators impose it by construction. This guarantees that nuisance variability is systematically removed from the learned features, preventing the model from encoding information that is irrelevant to the task. As a result, representational capacity is redirected toward modelling biologically meaningful variation, improving robustness, interpretability, and cross-dataset generalization. In the context of spherical biomedical data, invariant operators thus serve as a principled mechanism for disentangling biological signal from acquisition- and coordinate-induced artefacts, ensuring that other learning is driven by other scientifically relevant information.

4.2.3 Anisotropic Operator from $G(\mathbf{u} \cdot R\mathbf{d})$

Motivation: Neural tissue, cortical folding patterns, and white-matter fiber architectures exhibit pronounced directional structure that plays a fundamental role in their function and organization. These anisotropic systems with preferred directions exhibit different properties along different directions. Such anisotropy reflects direct heterogeneity of underlying biological mechanisms. Modelling these systems with operators that assume isotropic $SO(3)$ -symmetry can impose overly restrictive symmetry assumptions, forcing the model to treat all rotations as equally valid transformations. In many real-world systems, however, directional preferences, local reference frames, or constrained rotational freedoms are intrinsic to the underlying physical or semantic structure. Enforcing full equivariance in such cases can suppress direction-dependent responses, reduce representational flexibility, and lead to the loss of critical anisotropic information. Anisotropic operators are motivated by the need to model systems whose symmetries are inherently partial, directional, or locally constrained, rather than globally isotropic while retaining sphere-nativity. They provide a controlled and interpretable way to incorporate biologically meaningful anisotropy into the model.

Modeling Axisymmetric Anisotropic Systems: To explicitly model anisotropy, we draw inspiration from structures commonly found in nature that possess a single dominant orientation. A prime example is the 'white matter tract' in the brain, which consists of bundles of parallel neural fibers, akin to bundles of aligned cables. These tracts allow neural signals to propagate rapidly along the fiber orientation but hinder transverse propagation, thus establishing a clear 'preferred orientation'. Inspired by this, we propose a mathematical model, the anisotropic Green's function whose value depends solely on the angle between a spatial point \mathbf{u} and a rotatable 'preferred axis' $R\mathbf{d}$. Its mathematical form and harmonic extension:

$$G^A(u, R) = G^A(u \cdot (R\mathbf{d})) = \sum_{L \geq 0} g_L P_L(u \cdot (R\mathbf{d})), \quad (14)$$

where, P_L is the L -th order Legendre polynomial, and g_L are coefficients that determine the specific shape of the function. R represents a rotation applied to the system input. G_1 describes a system whose response resembles 'stacked thin sheets': it varies along the $R\mathbf{d}$ axis but remains completely uniform across the entire plane perpendicular to that axis. This perfectly captures anisotropy with rotational symmetry around a single axis.

Generalization to Broad Anisotropic Systems: To model more general anisotropy, we further allow different learnable preferred orientations \mathbf{d}_L for each spherical harmonic degree L . This yields a generalized anisotropic Green's function:

$$G^A(u \cdot (R\mathbf{d})) \rightarrow \sum_{L \geq 0} g_L P_L(\mathbf{u} \cdot (R\mathbf{d}_L)), \quad (15)$$

where each L -th order component is symmetric about its own axis $R\mathbf{d}_L$. The generalized form reduces to the axisymmetric form Equation 14 when all preferred directions are aligned, i.e., $\mathbf{d}_L = \mathbf{d}$ for all L .

Symmetry Analysis: The systems defined by G^A embody a special design that intertwines equivariance and invariance, which is precisely the mathematical origin of their ability to characterize "anisotropy". Specifically, the systems are invariant under rotations around their intrinsic (or per-degree) preferred axis \mathbf{d} (or \mathbf{d}_L), as such rotations do not alter the relative relationship between \mathbf{u} and $R\mathbf{d}$. However, they are equivariant under other rotation not centered on that preferred axis—a rotation R of the input source induces a coordinated rotation of the system's entire response pattern. This orientation-preferred symmetry reflects the intrinsic nature of physical anisotropy. Therefore, by endowing different frequency (angular momentum) components with independent directional degrees of freedom, G^A achieves learnable $SO(\theta)$ -symmetry, providing a powerful and theoretically grounded approach for modeling complex anisotropic responses.

We substitute this expansion into the integrand and define the inner integral $I_{\text{inner}}(R)$ by the Legendre expansion:

$$\begin{aligned}
I &= \int_{SO(3)} f(Rn) \left(\int_{S^2} [G(\mathbf{u} \cdot (R\mathbf{d}))] \overline{Y_\ell^m(u)} du \right) dR \\
&= \int_{SO(3)} f(Rn) \left(\int_{S^2} \left[\sum_{L \geq 0} g_L P_L(u \cdot (R\mathbf{d}_L)) \right] \overline{Y_\ell^m(u)} du \right) dR \\
&= \int_{SO(3)} f(Rn) I_{\text{inner}}(R) dR. \tag{16}
\end{aligned}$$

We solve the inner integral by applying the spherical harmonic addition theorem to each Legendre term:

$$\begin{aligned}
I_{\text{inner}}(R) &= \int_{S^2} \left[\sum_{L \geq 0} g_L P_L(u \cdot (R\mathbf{d}_L)) \right] \overline{Y_\ell^m(u)} du \\
&= \sum_{L \geq 0} g_L \int_{S^2} P_L(u \cdot (R\mathbf{d}_L)) \overline{Y_\ell^m(u)} du \\
&= \sum_{L \geq 0} g_L \frac{4\pi}{2L+1} \sum_{m'=-L}^L \overline{Y_L^{m'}(R\mathbf{d}_L)} \int_{S^2} Y_L^{m'}(u) \overline{Y_\ell^m(u)} du \\
&= \sum_{L \geq 0} g_L \frac{4\pi}{2L+1} \sum_{m'=-L}^L \overline{Y_L^{m'}(R\mathbf{d}_L)} \delta_{L\ell} \delta_{m'm} \\
&= g_\ell \frac{4\pi}{2\ell+1} \overline{Y_\ell^m(R\mathbf{d}_\ell)}. \tag{17}
\end{aligned}$$

Based on the transformation law of spherical harmonics under rotations together with the orthogonality of Wigner D -matrices over $SO(3)$ equipped with the normalized

Haar measure, we substitute the inner result back into the outer integral over $SO(3)$ and solve the final integral I by the harmonic expansion:

$$\begin{aligned}
I &= g_\ell \frac{4\pi}{2\ell+1} \cdot \int_{SO(3)} f(Rn) \overline{Y_\ell^m(Rd_l)} dR \\
&= g_\ell \frac{4\pi}{2\ell+1} \cdot \int_{SO(3)} f(R^{-1}n) \overline{Y_\ell^m(R^{-1}d_l)} dR \\
&= g_\ell \frac{4\pi}{2\ell+1} \cdot \int_{SO(3)} \left(\sum_{L,M} \text{SHT}[f]_L^M \sum_{a=-L}^L D_{aM}^{(L)}(R) Y_L^a(n) \right) \left(\sum_{b=-\ell}^{\ell} \overline{D_{bm}^{(\ell)}(R) Y_\ell^b(d_l)} \right) dR \\
&= g_\ell \frac{4\pi}{2\ell+1} \cdot \sum_{L,M} \sum_{a=-L}^L \sum_{b=-\ell}^{\ell} \text{SHT}[f]_L^M Y_L^a(n) \overline{Y_\ell^b(d_l)} \int_{SO(3)} D_{aM}^{(L)}(R) \overline{D_{bm}^{(\ell)}(R)} dR \\
&= g_\ell \frac{4\pi}{2\ell+1} \cdot \sum_{L,M} \sum_{a=-L}^L \sum_{b=-\ell}^{\ell} \text{SHT}[f]_L^M Y_L^a(n) \overline{Y_\ell^b(d_l)} \frac{1}{2\ell+1} \delta_{L\ell} \delta_{ab} \delta_{Mm} \\
&= g_\ell \frac{4\pi}{(2\ell+1)^2} \cdot \sum_{a=-\ell}^{\ell} \text{SHT}[f](\ell, m) Y_\ell^a(n) \overline{Y_\ell^a(d_l)} \\
&= g_\ell \frac{4\pi}{(2\ell+1)^2} \cdot \text{SHT}[f](\ell, m) \cdot \frac{2\ell+1}{4\pi} P_\ell(n \cdot d_l) \\
&= \frac{g_\ell \cdot \text{SHT}[f](\ell, m)}{2\ell+1} P_\ell(n \cdot d_l) \tag{18}
\end{aligned}$$

This final derived solution exhibits separation of variables: the dependence on the input f appears only through its spherical harmonic coefficient f_ℓ^m , while the geometric dependence on the two fixed directions n and d is captured entirely by $P_\ell(n \cdot d)$. Besides, the coefficient g_ℓ is also a symmetrical kernel. Therefore, in our fusing operator GSNO, the anisotropic operator solution is simplified to the core anisotropic component:

$$\text{SHT}[g(u)](\ell, m) = \text{SHT}[f](\ell, m) P_\ell(n \cdot \mathbf{d}_\theta). \tag{19}$$

where \mathbf{d}_θ is the learnable orientations. The anisotropic operators respect underlying geometric structure and allow the model to express distinct modes along distinct directions, reflecting the organization of biological substrates such as fiber tracts or cortical boundaries. Therefore, by explicitly modelling anisotropy where it is biologically warranted, the operators enable the capture of heterogeneous, structure-driven variation. They thus complement spherical operators by restoring expressivity in a principled and biologically grounded manner.

References

- [1] Rasp, S., Dueben, P.D., Scher, S., Weyn, J.A., Mouatadid, S., Thuerey, N.: Weatherbench: a benchmark data set for data-driven weather forecasting. *Journal of Advances in Modeling Earth Systems* **12**(11), 2020–002203 (2020)
- [2] Pathak, J., Subramanian, S., Harrington, P., Raja, S., Chattopadhyay, A., Mardani, M., Kurth, T., Hall, D., Li, Z., Azizzadenesheli, K., et al.: Fourcastnet: A global data-driven high-resolution weather model using adaptive fourier neural operators. arXiv preprint arXiv:2202.11214 (2022)
- [3] Bonev, B., Kurth, T., Hundt, C., Pathak, J., Baust, M., Kashinath, K., Anandkumar, A.: Spherical fourier neural operators: Learning stable dynamics on the sphere. In: *International Conference on Machine Learning*, pp. 2806–2823 (2023). PMLR
- [4] Liu, C., Hsu, K., Peng, M., Chen, D., Chang, P., Hsiao, L., et al.: Evaluation of five global AI models for predicting weather in Eastern Asia and Western Pacific. *npj Climate and Atmospheric Science*, 7 (1), 221 (2024)
- [5] Hu, Y., Yin, F., Zhang, W., Ren, K., Song, J., Deng, K., Zhang, D.: Spherical multigrid neural operator for improving autoregressive global weather forecasting. *Scientific Reports* **15**(1), 11522 (2025)
- [6] Zhao, F., Xia, S., Wu, Z., Duan, D., Wang, L., Lin, W., Gilmore, J.H., Shen, D., Li, G.: Spherical u-net on cortical surfaces: methods and applications. In: *International Conference on Information Processing in Medical Imaging*, pp. 855–866 (2019). Springer
- [7] Zhao, F., Wu, Z., Wang, L., Lin, W., Gilmore, J.H., Xia, S., Shen, D., Li, G.: Spherical deformable u-net: Application to cortical surface parcellation and development prediction. *IEEE transactions on medical imaging* **40**(4), 1217–1228 (2021)
- [8] Elaldi, A., Dey, N., Kim, H., Gerig, G.: Equivariant spherical deconvolution: Learning sparse orientation distribution functions from spherical data. In: *International Conference on Information Processing in Medical Imaging*, pp. 267–278 (2021). Springer
- [9] Ha, S., Lyu, I.: Spharm-net: Spherical harmonics-based convolution for cortical parcellation. *IEEE Transactions on Medical Imaging* **41**(10), 2739–2751 (2022)
- [10] Elaldi, A., Gerig, G., Dey, N.: Equivariant spatio-hemispherical networks for diffusion mri deconvolution. *Advances in Neural Information Processing Systems* **37**, 52095–52126 (2024)
- [11] Sedlar, S., Papadopoulou, T., Deriche, R., Deslauriers-Gauthier, S.: Diffusion mri

- fiber orientation distribution function estimation using voxel-wise spherical u-net. In: Computational Diffusion MRI: International MICCAI Workshop, Lima, Peru, October 2020, pp. 95–106 (2021). Springer
- [12] Sedlar, S., Alimi, A., Papadopoulos, T., Deriche, R., Deslauriers-Gauthier, S.: A spherical convolutional neural network for white matter structure imaging via dmri. In: International Conference on Medical Image Computing and Computer-Assisted Intervention, pp. 529–539 (2021). Springer
- [13] Su, Y.-C., Grauman, K.: Learning spherical convolution for fast features from 360 imagery. *Advances in neural information processing systems* **30** (2017)
- [14] Zhang, Z., Xu, Y., Yu, J., Gao, S.: Saliency detection in 360 videos. In: Proceedings of the European Conference on Computer Vision (ECCV), pp. 488–503 (2018)
- [15] Wu, C., Zhang, R., Wang, Z., Sun, L.: A spherical convolution approach for learning long term viewport prediction in 360 immersive video. In: Proceedings of the AAAI Conference on Artificial Intelligence, vol. 34, pp. 14003–14040 (2020)
- [16] Su, Y.-C., Grauman, K.: Learning spherical convolution for 360° recognition. *IEEE Transactions on Pattern Analysis and Machine Intelligence* **44**(11), 8371–8386 (2021)
- [17] Xu, Y., Zhang, Z., Gao, S.: Spherical dnns and their applications in 360° images and videos. *IEEE Transactions on Pattern Analysis and Machine Intelligence* **44**(10), 7235–7252 (2021)
- [18] Boomsma, W., Frelsen, J.: Spherical convolutions and their application in molecular modelling. *Advances in neural information processing systems* **30** (2017)
- [19] Cohen, T.S., Geiger, M., Köhler, J., Welling, M.: Spherical cnns. arXiv preprint arXiv:1801.10130 (2018)
- [20] Kondor, R., Lin, Z., Trivedi, S.: Clebsch–gordan nets: a fully fourier space spherical convolutional neural network. *Advances in Neural Information Processing Systems* **31** (2018)
- [21] Cobb, O.J., Wallis, C.G., Mavor-Parker, A.N., Marignier, A., Price, M.A., d’Avezac, M., McEwen, J.D.: Efficient generalized spherical cnns. arXiv preprint arXiv:2010.11661 (2020)
- [22] Esteves, C., Slotine, J.-J., Makadia, A.: Scaling spherical cnns. arXiv preprint arXiv:2306.05420 (2023)
- [23] Su, Q., Zhang, H., Gou, Q., Sun, H., Fang, M., Zhang, X., Hu, R., Kang, Y., Hsieh,

- C.-Y., Wang, J., *et al.*: Lumicharge: Spherical harmonic convolutional networks for atomic charge prediction in drug discovery. *The Journal of Physical Chemistry Letters* **16**, 6334–6344 (2025)
- [24] Xu, Y., Xiao, T., Zhang, J., Yang, K., Zhang, Z.: Scale-invariant convolutional neural networks. *arXiv preprint arXiv:1411.6369* (2014)
- [25] Ronneberger, O., Fischer, P., Brox, T.: U-Net: Convolutional networks for biomedical image segmentation. In: *Medical Image Computing and Computer-Assisted Intervention*, pp. 234–241 (2015). Springer
- [26] Maron, H., Galun, M., Aigerman, N., Trope, M., Dym, N., Yumer, E., Kim, V.G., Lipman, Y.: Convolutional neural networks on surfaces via seamless toric covers. *ACM Trans. Graph.* **36**(4), 71–1 (2017)
- [27] Coors, B., Condurache, A.P., Geiger, A.: Spherenet: Learning spherical representations for detection and classification in omnidirectional images. In: *Proceedings of the European Conference on Computer Vision (ECCV)*, pp. 518–533 (2018)
- [28] Park, S.W., Kwon, J.: Spheregans: Sphere generative adversarial network based on geometric moment matching and its applications. *IEEE Transactions on Pattern Analysis and Machine Intelligence* **44**(3), 1566–1580 (2020)
- [29] Cohen, T., Welling, M.: Group equivariant convolutional networks. In: *International Conference on Machine Learning*, pp. 2990–2999 (2016). PMLR
- [30] Bronstein, M.M., Bruna, J., Cohen, T., Velicković, P.: Geometric deep learning: Grids, groups, graphs, geodesics, and gauges. *arXiv preprint arXiv:2104.13478* (2021)
- [31] Rao, Y., Lu, J., Zhou, J.: Spherical fractal convolutional neural networks for point cloud recognition. In: *Proceedings of the IEEE/CVF Conference on Computer Vision and Pattern Recognition*, pp. 452–460 (2019)
- [32] Perraudin, N., Defferrard, M., Kacprzak, T., Sgier, R.: Deepsphere: Efficient spherical convolutional neural network with healpix sampling for cosmological applications. *Astronomy and Computing* **27**, 130–146 (2019)
- [33] Defferrard, M., Milani, M., Gusset, F., Perraudin, N.: Deepsphere: a graph-based spherical cnn. *arXiv preprint arXiv:2012.15000* (2020)
- [34] Perry, S., Yin, M.S., Gray, K., Kobourov, S.: Drawing graphs on the sphere. In: *Proceedings of the 2020 International Conference on Advanced Visual Interfaces*, pp. 1–9 (2020)
- [35] Lei, H., Akhtar, N., Mian, A.: Spherical kernel for efficient graph convolution on 3d point clouds. *IEEE transactions on pattern analysis and machine intelligence*

43(10), 3664–3680 (2020)

- [36] Liu, Y., Wang, L., Liu, M., Zhang, X., Oztekin, B., Ji, S.: Spherical message passing for 3d graph networks. arXiv preprint arXiv:2102.05013 (2021)
- [37] Su, Y.-C., Grauman, K.: Kernel transformer networks for compact spherical convolution. In: Proceedings of the IEEE/CVF Conference on Computer Vision and Pattern Recognition, pp. 9442–9451 (2019)
- [38] Cho, S., Jung, R., Kwon, J.: Spherical transformer. arXiv preprint arXiv:2202.04942 (2022)
- [39] Cheng, J., Zhang, X., Zhao, F., Wu, Z., Yuan, X., Gilmore, J.H., Wang, L., Lin, W., Li, G.: Spherical transformer on cortical surfaces. In: International Workshop on Machine Learning in Medical Imaging, pp. 406–415 (2022). Springer
- [40] Lai, X., Chen, Y., Lu, F., Liu, J., Jia, J.: Spherical transformer for lidar-based 3d recognition. In: Proceedings of the IEEE/CVF Conference on Computer Vision and Pattern Recognition, pp. 17545–17555 (2023)
- [41] Carlsson, O., Gerken, J.E., Linander, H., Spieß, H., Ohlsson, F., Petersson, C., Persson, D.: Heal-swin: A vision transformer on the sphere. In: Proceedings of the IEEE/CVF Conference on Computer Vision and Pattern Recognition, pp. 6067–6077 (2024)
- [42] Zhang, J., Chen, Z., Lin, C., Shen, Z., Nie, L., Liao, K., Zhao, Y.: Sgformer: Spherical geometry transformer for 360 depth estimation. IEEE Transactions on Circuits and Systems for Video Technology (2025)
- [43] Benny, Y., Wolf, L.: Sphereformer: A u-shaped transformer for spherical 360 perception. In: Proceedings of the Computer Vision and Pattern Recognition Conference, pp. 940–950 (2025)
- [44] Volkovs, K., Urtans, E., Caune, V.: Primed unet-lstm for weather forecasting. In: Proceedings of the 2023 7th International Conference on Advances in Artificial Intelligence, pp. 13–17 (2023)
- [45] Liu, M., Yao, F., Choi, C., Sinha, A., Ramani, K.: Deep learning 3d shapes using alt-az anisotropic 2-sphere convolution. In: International Conference on Learning Representations (2018)
- [46] Cohen, T., Geiger, M., Köhler, J., Welling, M.: Convolutional networks for spherical signals. arXiv preprint arXiv:1709.04893 (2017)
- [47] Driscoll, J.R., Healy, D.M.: Computing fourier transforms and convolutions on the 2-sphere. *Advances in applied mathematics* **15**(2), 202–250 (1994)
- [48] Wandelt, B.D., Górski, K.M.: Fast convolution on the sphere. *Physical review D*

63(12), 123002 (2001)

- [49] Jiang, C., Huang, J., Kashinath, K., Marcus, P., Niessner, M., et al.: Spherical cnns on unstructured grids. arXiv preprint arXiv:1901.02039 (2019)
- [50] Lee, S., Lee, S., Willbrand, E.H., Parker, B.J., Bunge, S.A., Weiner, K.S., Lyu, I.: Leveraging input-level feature deformation with guided-attention for sulcal labeling. *IEEE Transactions on Medical Imaging* (2024)
- [51] You, S., De Leon Barba, A., Cruz Tamayo, V., Yun, H.J., Yang, E., Grant, P.E., Im, K.: Automatic cortical surface parcellation in the fetal brain using attention-gated spherical u-net. *Frontiers in Neuroscience* **18**, 1410936 (2024)
- [52] Lee, S., Lee, S., Ryu, S., Lyu, I.: Spharm-reg: Unsupervised cortical surface registration using spherical harmonics. *IEEE Transactions on Medical Imaging* (2025)
- [53] Elaldi, A., Gerig, G., Dey, N.: E (3) x so (3)-equivariant networks for spherical deconvolution in diffusion mri. In: *Medical Imaging with Deep Learning*, pp. 301–319 (2024). PMLR
- [54] Lin, K., Li, X., Ye, Y., Feng, S., Zhang, B., Xu, G., Wang, Z.: Spherical neural operator network for global weather prediction. *IEEE Transactions on Circuits and Systems for Video Technology* **34**(6), 4899–4913 (2023)
- [55] Mahesh, A., Collins, W., Bonev, B., Brenowitz, N., Cohen, Y., Elms, J., Harrington, P., Kashinath, K., Kurth, T., North, J., et al.: Huge ensembles part i: Design of ensemble weather forecasts using spherical fourier neural operators. arXiv preprint arXiv:2408.03100 (2024)
- [56] Mahesh, A., Collins, W., Bonev, B., Brenowitz, N., Cohen, Y., Harrington, P., Kashinath, K., Kurth, T., North, J., O'Brien, T., et al.: Huge ensembles part ii: Properties of a huge ensemble of hindcasts generated with spherical fourier neural operators. arXiv preprint arXiv:2408.01581 (2024)
- [57] Zhang, Z., Wang, Y.: A global earthquake prediction model based on spherical convolutional lstm. *IEEE Transactions on Geoscience and Remote Sensing* **62**, 1–10 (2024)
- [58] Edmonds, A.R.: *Angular Momentum in Quantum Mechanics* vol. 4. Princeton university press, ??? (1996)
- [59] Müller, C.: *Spherical Harmonics* vol. 17. Springer, ??? (2006)
- [60] Tang, H., Zhu, J., Feng, Z., Li, H., Li, C.: Geometric laplace neural operator. arXiv preprint arXiv:2512.16409 (2025)
- [61] Stakgold, I., Holst, M.J.: *Green's Functions and Boundary Value Problems*. John

Wiley & Sons, Canada (2011)

- [62] Lucarini, V., Chekroun, M.D.: Detecting and attributing change in climate and complex systems: Foundations, green’s functions, and nonlinear fingerprints. *Physical Review Letters* **133**(24), 244201 (2024)
- [63] Behroozi, A., Shen, C., Kifer, D.: Sensitivity-constrained fourier neural operators for forward and inverse problems in parametric differential equations. In: *The Thirteenth International Conference on Learning Representations* (2025)
- [64] Giambagli, L., Buffoni, L., Carletti, T., Nocentini, W., Fanelli, D.: Machine learning in spectral domain. *Nature communications* **12**(1), 1330 (2021)
- [65] Wang, R., Walters, R., Yu, R.: Approximately equivariant networks for imperfectly symmetric dynamics. In: *International Conference on Machine Learning*, pp. 23078–23091 (2022). PMLR
- [66] Pertigkiozoglou, S., Chatzipantazis, E., Trivedi, S., Daniilidis, K.: Improving equivariant model training via constraint relaxation. *Advances in Neural Information Processing Systems* **37**, 83497–83520 (2024)
- [67] Huang, W., Han, J., Rong, Y., Xu, T., Sun, F., Huang, J.: Equivariant graph mechanics networks with constraints. *arXiv preprint arXiv:2203.06442* (2022)
- [68] Duval, A.A., Schmidt, V., Hernández-García, A., Miret, S., Malliaros, F.D., Bengio, Y., Rolnick, D.: Faenet: Frame averaging equivariant gnn for materials modeling. In: *International Conference on Machine Learning*, pp. 9013–9033 (2023). PMLR
- [69] Zheng, Z., Liu, Y., Li, J., Yao, J., Rong, Y.: Relaxing continuous constraints of equivariant graph neural networks for broad physical dynamics learning. In: *Proceedings of the 30th ACM SIGKDD Conference on Knowledge Discovery and Data Mining*, pp. 4548–4558 (2024)
- [70] Li, Z., Zheng, H., Kovachki, N., Jin, D., Chen, H., Liu, B., Azizzadenesheli, K., Anandkumar, A.: Physics-informed neural operator for learning partial differential equations. *ACM/IMS Journal of Data Science* **1**(3), 1–27 (2024)
- [71] Tang, H., Chen, H., Li, C.: Generalized spherical neural operators: Green’s function formulation. *arXiv preprint arXiv:2512.10723* (2025)
- [72] Bonev, B., Hesthaven, J.S., Giraldo, F.X., Koper, M.A.: Discontinuous galerkin scheme for the spherical shallow water equations with applications to tsunami modeling and prediction. *Journal of Computational Physics* **362**, 425–448 (2018)
- [73] Giraldo, F.X.: A spectral element shallow water model on spherical geodesic grids. *International Journal for Numerical Methods in Fluids* **35**(8), 869–901 (2001)

- [74] Khan, W., Egorova, N., Khlif, M.S., Mito, R., Dhollander, T., Brodtmann, A.: Three-tissue compositional analysis reveals in-vivo microstructural heterogeneity of white matter hyperintensities following stroke. *Neuroimage* **218**, 116869 (2020)
- [75] Zeng, R., Lv, J., Wang, H., Zhou, L., Barnett, M., Calamante, F., Wang, C.: Fod-net: A deep learning method for fiber orientation distribution angular super resolution. *Medical Image Analysis* **79**, 102431 (2022)
- [76] Snoussi, H., Karimi, D.: Equivariant spherical cnns for accurate fiber orientation distribution estimation in neonatal diffusion mri with reduced acquisition time. *arXiv preprint arXiv:2504.01925* (2025)
- [77] Van Essen, D.C., Smith, S.M., Barch, D.M., Behrens, T.E., Yacoub, E., Ugurbil, K., Consortium, W.-M.H., *et al.*: The wu-minn human connectome project: an overview. *Neuroimage* **80**, 62–79 (2013)
- [78] Jeurissen, B., Tournier, J.-D., Dhollander, T., Connelly, A., Sijbers, J.: Multi-tissue constrained spherical deconvolution for improved analysis of multi-shell diffusion mri data. *NeuroImage* **103**, 411–426 (2014)
- [79] Klein, A., Tourville, J.: 101 labeled brain images and a consistent human cortical labeling protocol. *Frontiers in neuroscience* **6**, 171 (2012)
- [80] Desikan, R.S., Ségonne, F., Fischl, B., Quinn, B.T., Dickerson, B.C., Blacker, D., Buckner, R.L., Dale, A.M., Maguire, R.P., Hyman, B.T., *et al.*: An automated labeling system for subdividing the human cerebral cortex on mri scans into gyral based regions of interest. *Neuroimage* **31**(3), 968–980 (2006)
- [81] Blum, L.C., Raymond, J.-L.: 970 million druglike small molecules for virtual screening in the chemical universe database gdb-13. *Journal of the American Chemical Society* **131**(25), 8732–8733 (2009)
- [82] Rupp, M., Tkatchenko, A., Müller, K.-R., Von Lilienfeld, O.A.: Fast and accurate modeling of molecular atomization energies with machine learning. *Physical review letters* **108**(5), 058301 (2012)
- [83] Li, Z., Kovachki, N., Azizzadenesheli, K., Liu, B., Bhattacharya, K., Stuart, A., Anandkumar, A.: Neural operator: Graph kernel network for partial differential equations. *arXiv preprint arXiv:2003.03485* (2020)